

Thermal properties of graphene under tensile stress

Carlos P. Herrero and Rafael Ramírez

Instituto de Ciencia de Materiales de Madrid, Consejo Superior de Investigaciones Científicas (CSIC), Campus de Cantoblanco, 28049 Madrid, Spain

(Dated: June 7, 2018)

Thermal properties of graphene display peculiar characteristics associated to the two-dimensional nature of this crystalline membrane. These properties can be changed and tuned in the presence of applied stresses, both tensile and compressive. Here we study graphene monolayers under tensile stress by using path-integral molecular dynamics (PIMD) simulations, which allows one to take into account quantization of vibrational modes and analyze the effect of anharmonicity on physical observables. The influence of the elastic energy due to strain in the crystalline membrane is studied for increasing tensile stress and for rising temperature (thermal expansion). We analyze the internal energy, enthalpy, and specific heat of graphene, and compare the results obtained from PIMD simulations with those given by a harmonic approximation for the vibrational modes. This approximation turns out to be precise at low temperatures, and deteriorates as temperature and pressure are increased. At low temperature the specific heat changes as $c_p \sim T$ for stress-free graphene, and evolves to a dependence $c_p \sim T^2$ as the tensile stress is increased. Structural and thermodynamic properties display nonnegligible quantum effects, even at temperatures higher than 300 K. Moreover, differences in the behavior of the in-plane and real areas of graphene are discussed, along with their associated properties. These differences show up clearly in the corresponding compressibility and thermal expansion coefficient.

PACS numbers: 61.48.Gh, 65.80.Ck, 63.22.Rc

I. INTRODUCTION

Two-dimensional materials, and graphene in particular, have attracted in last years a great deal of attention in the scientific community, due to their peculiar electronic, elastic, and thermal properties.^{1–3} Thus, graphene presents high values of the thermal conductivity,^{4,5} and large in-plane elastic constants.⁶ Moreover, its mechanical properties are interesting for possible applications, as cooling of electronic devices.^{7,8}

The ideal structure of pure defect-free graphene is a planar honeycomb lattice, but departures from this flat configuration may appreciably alter its atomic-scale and macroscopic properties.⁹ Several reasons can cause bending of a graphene sheet, such as the presence of defects and external stresses.¹⁰ In addition, thermal fluctuations at finite temperatures give rise to out-of-plane displacements of the C atoms, and for $T \rightarrow 0$, zero-point motion yields also a departure of strict planarity of the graphene sheet.¹¹

The influence of strain in several characteristics of two-dimensional (2D) materials, such as graphene and metallic dichalcogenides, has been emphasized in recent years. This includes electronic transport, optical properties, and the formation of moiré patterns.^{12,13} From a structural viewpoint, external stresses may cause significant changes in crystalline membranes, which can crumple in the presence of a compressive stress, as is well known for lipid membranes^{14,15} and polymer films.^{16,17} For graphene, crumpling was observed in supported as well as freestanding samples, and has been explained as due to both out-of-plane phonons and static wrinkling.^{18,19} Recent molecular dynamics simulations indicate that the maximum compressive stress that a

freestanding graphene sheet can sustain without crumpling decreases as the system size grows, and was estimated to be about 0.1 N/m at room temperature in the thermodynamic limit.²⁰

A tensile stress in the graphene plane does not break the planarity of the sheet, but gives rise to significant variations in the elastic properties of the material.²¹ For example, the in-plane Young modulus increases by a factor of three for a tensile stress of 1 N/m.²⁰ In this respect, the real area per atom, A , can be crucial to understand the elastic properties, which have been in the past usually referred to its projection, A_p , onto the mean plane of the membrane ($A_p \leq A$). This question has been discussed along the years for biological membranes,^{15,22–25} and has been recently examined for crystalline membranes such as graphene.^{11,19,26–28} In particular, the high-quality data obtained by Nicholl *et al.*^{19,27} clearly indicate that some experimental techniques can measure properties related to the real area A , whereas other techniques may be used to quantify variables connected to the projected area A_p . The difference $A - A_p$ has been called *hidden* area for graphene in Ref. 27, as well as *excess* area for biological membranes.^{22,23} A precise knowledge of the behavior of both areas is important to clarify the temperature and stress dependence of structural and thermodynamic properties of graphene. Thus, it is possible to define the elastic properties in relation to the area A or to A_p , which may behave very differently. In fact, it is known that referring to the in-plane area A_p , one finds a negative thermal expansion coefficient, but for the real area A the thermal expansion is positive.^{11,26}

A deep comprehension of the properties of 2D systems has been for many years a persistent goal in statistical physics.^{15,24,29} This has been in part due to the complex-

ity of the considered systems, such as biological membranes and soft condensed matter.^{24,25} In this respect, graphene can be dealt with as a model system where descriptions at an atomic level can be connected with physical properties of the material. Thus, thermal properties of graphene have been investigated in recent years,^{30–34} and in particular its thermal expansion and heat conduction were studied by various theoretical and experimental techniques.^{4,31,35–38}

Several theoretical works carried out to study thermodynamic properties of graphene (e.g., specific heat, thermal expansion, ...), were based on density-functional-theory (DFT) calculations combined with a quantum quasi-harmonic approximation (QHA) for the vibrational modes.^{39–41} This is expected to yield reliable results at low temperature, but may be questioned at relatively high temperature, especially for the thermal expansion, due to an important anharmonic coupling between in-plane and out-of-plane modes, not included in the QHA. Moreover, classical Monte Carlo and molecular dynamics simulations based on *ab-initio*,^{26,42–44} tight-binding,^{45–48} and empirical potentials^{10,28,49,50} can give reliable results at relatively high temperature, but fail to describe thermodynamic properties at $T < \Theta_D$, with $\Theta_D \gtrsim 1000$ K the Debye temperature of the material. This means, in particular, that room-temperature results obtained for some properties of graphene from classical atomistic simulations may be clearly unrealistic. These shortcuts may be overcome by using simulation methods which explicitly include nuclear quantum effects, in particular those based on Feynman path integrals.^{11,51–53}

Here we use the path-integral molecular dynamics (PIMD) method to study thermal properties of graphene under tensile stress at temperatures between 12 and 2000 K. The thermal behavior of the graphene surface is studied, considering the difference between in-plane and real areas. The in-plane thermal expansion coefficient turns out to be negative at low temperatures, with a crossing to positive values at a temperature which decreases fast as tensile stress is raised. Particular emphasis is laid on the temperature dependence of the specific heat at low T , for which results of the simulations are compared with predictions based on harmonic vibrations of the crystalline membrane. This approximation happens to be noticeably accurate at low temperatures, once the frequencies of out-of-plane ZA modes are properly renormalized for changing applied stress.

The paper is organized as follows. In Sec. II we describe the computational method employed in the simulations. Results for the internal energy and enthalpy of graphene are given in Sec. III. The thermal expansion is discussed in Sec. IV. In Sec. V we present results for the specific heat, whereas in Sec. VI the compressibility of graphene is discussed. In Sec. VII we summarize the main results.

II. COMPUTATIONAL METHOD

A. Path-integral molecular dynamics

We use PIMD simulations to study equilibrium properties of graphene monolayers as a function of temperature and pressure. The PIMD procedure is based on the Feynman path-integral formulation of statistical mechanics,⁵⁴ an adequate nonperturbative approach to study finite-temperature properties of many-body quantum systems. In the applications of this method to numerical simulations, each quantum particle is represented by a set of N_{Tr} (Trotter number) replicas (or beads), that behave as classical-like particles forming a ring polymer.^{51,52} Thus, one deals with a *classical isomorph* whose dynamics is artificial, since it does not reflect the real quantum dynamics of the actual particles, but is useful for effectively sampling the many-body configuration space, yielding precise results for time-independent equilibrium properties of the quantum system. Details on this type of simulation techniques are given in Refs. 51,52,55,56.

The interatomic interactions between carbon atoms are described here by using the LCBOP-II effective potential, a long-range bond order potential, which has been mainly employed to carry out classical simulations of carbon-based systems.⁵⁷ In particular, it was used to study the phase diagram of carbon, including graphite, diamond, and the liquid, and showed its accuracy in predicting rather precisely the graphite-diamond transition line.⁵⁸ In recent years, this interatomic potential has been also found to describe well several properties of graphene,^{10,50} and its Young's modulus in particular.^{20,59,60} This interatomic potential was lately employed to carry out PIMD simulations, which allowed to quantify quantum effects in graphene monolayers by comparing with results of classical simulations,¹¹ as well as to study thermodynamic properties of this 2D material.⁶¹ Here, in line with earlier simulations,^{11,20,28} the original parameterization of the LCBOP-II potential has been slightly changed to rise the zero-temperature bending constant κ from 1.1 eV to 1.49 eV, a value close to experimental data.⁶²

The calculations presented here have been performed in the isothermal-isobaric ensemble, where one fixes the number of carbon atoms (N), the applied stress (P), and the temperature (T). The stress P in the reference xy plane of graphene, with units of force per unit length, coincides with the so-called mechanical or frame tension.^{20,23,63} P is obtained in the simulations from the stress tensor τ , whose components are given by expressions such as^{61,64}

$$\tau_{xy} = \left\langle \frac{1}{NA_p} \left(\sum_{i=1}^N \sum_{j=1}^{N_{\text{Tr}}} (m_j v_{ij,x} v_{ij,y} - 2k_j u_{ij,x} u_{ij,y}) - \frac{1}{N_{\text{Tr}}} \sum_{j=1}^{N_{\text{Tr}}} \frac{\partial U(\mathbf{r}_{1j}, \dots, \mathbf{r}_{Nj})}{\partial \epsilon_{xy}} \right) \right\rangle, \quad (1)$$

where the brackets $\langle \dots \rangle$ indicate an ensemble average and \mathbf{u}_{ij} are staging coordinates,⁶⁵ with $i = 1, \dots, N$ and $j = 1, \dots, N_{\text{Tr}}$. In Eq. (1), m_j is the dynamic mass associated to \mathbf{u}_{ij} and $v_{ij,x}$, $v_{ij,y}$ are components of its corresponding velocity. The constant k_j is given by $k_j = m_j N_{\text{Tr}} / 2\beta^2 \hbar^2$ for $j > 1$ and $k_1 = 0$. Here $\beta = (k_B T)^{-1}$, U is the instantaneous potential energy, and ϵ_{xy} is an element of the 2D strain tensor. The stress P , conjugate to the in-plane area A_p , is given by the trace of the stress tensor:

$$P = \frac{1}{2} (\tau_{xx} + \tau_{yy}). \quad (2)$$

Effective algorithms have been employed for the PIMD simulations, as those described in the literature.^{64,66,67} In particular, a constant temperature T was accomplished by coupling chains of four Nosé-Hoover thermostats, and an additional chain of four barostats was coupled to the area of the graphene simulation box to yield the required stress P .^{55,64} The equations of motion were integrated by employing the reversible reference system propagator algorithm (RESPA), allowing to define different time steps for the integration of the fast and slow degrees of freedom.⁶⁸ The kinetic energy K has been calculated by using the virial estimator, which displays a statistical uncertainty significantly smaller than the potential energy, $V = \langle U \rangle$.⁶⁴ The time step Δt associated to the interatomic forces has been taken as 0.5 fs, which was found to be suitable for the carbon atomic mass and the temperature range considered here. More details on this kind of PIMD simulations can be found elsewhere.^{64,69,70}

Rectangular simulation cells with $N = 960$ atoms have been considered, with similar side lengths in the x and y directions ($L_x \approx L_y \approx 50 \text{ \AA}$), and periodic boundary conditions were assumed. Sampling of the configuration space was performed in the temperature range between 12 K and 2000 K. A temperature-dependent Trotter number has been defined as $N_{\text{Tr}} = 6000\text{K}/T$, which yields a roughly constant precision for the PIMD results at different temperatures.⁶⁹⁻⁷¹ Given a temperature T and a stress P , a typical simulation run included 3×10^5 PIMD steps for system equilibration and 6×10^6 steps for calculation of average properties.

B. In-plane vs real area

As explained above, in the isothermal-isobaric ensemble used here we fix the applied stress P in the xy plane, allowing fluctuations in the in-plane area of the simulation cell for which periodic boundary conditions are ap-

plied. Carbon atoms are free to move in the z coordinate (out-of-plane direction), and in general any measure of the *real* surface of a graphene sheet at $T > 0$ should give a value larger than the in-plane area. In this respect, it has been discussed for biological membranes that their properties should be described using the notion of a real surface rather than a *projected* (in-plane) surface.^{25,72} A similar question has been also recently posed for crystalline membranes such as graphene.^{11,20,26,27} This may be relevant for addressing the calculation of thermodynamic variables, as the in-plane area A_p is the variable conjugate to the stress P used in our simulations. The real area (also called true, actual, or effective area in the literature^{23,25,72}) is conjugate to the usually-called surface tension.¹⁵

The in-plane area has been most used to present the results of atomistic simulations of graphene layers.^{25,50,53,59,73} For biological membranes, however, it has been shown that values of the compressibility may significantly differ when they are related to A or to A_p , and something similar has been recently found for the elastic properties of graphene from classical molecular dynamics simulations.²⁰

Here we calculate a *real* area A in three-dimensional (3D) space by a triangulation based on the actual positions of the C atoms along a simulation run (in fact we use the beads associated to the atomic nuclei). Specifically, A is obtained from a sum of areas corresponding to the structural hexagons. Each hexagon contributes as a sum of six triangles, each one formed by the positions of two adjacent C atoms and the barycenter of the hexagon.²⁰

The instantaneous area per atom for *imaginary time* (bead) j is given by

$$A^j = \frac{1}{N} \sum_{k=1}^{2N} \sum_{n=1}^6 T_{kn}^j \quad (3)$$

where T_{kn}^j is the area of triangle n in hexagon k , and the sum in k is extended to the $2N$ hexagons in a cell containing N carbon atoms. Here, the triangles are defined with the coordinates \mathbf{r}_{ij} corresponding to bead j of atom i . The area A is then calculated as

$$A = \left\langle \frac{1}{N_{\text{Tr}}} \sum_{j=1}^{N_{\text{Tr}}} A^j \right\rangle \quad (4)$$

It is clear that A coincides with A_p for strictly planar graphene, and in general one has $A \geq A_p$. Both areas display temperature dependencies qualitatively different.

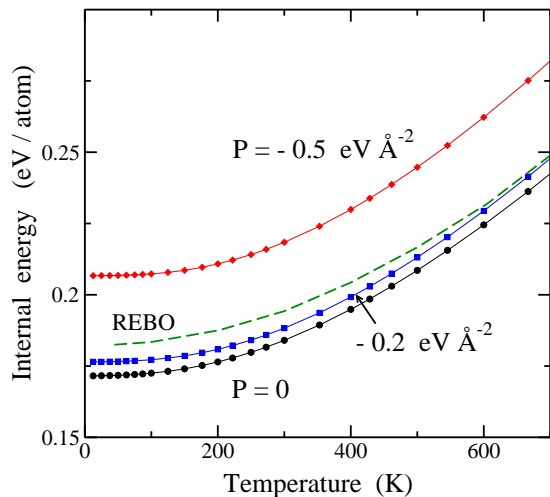


FIG. 1: Internal energy per atom $E - E_0$ as a function of temperature for $P = 0$ (circles), -0.2 (squares), and -0.5 eV \AA^{-2} (diamonds). Symbols represent results of PIMD simulations. Error bars are smaller than the symbol size. Solid lines are guides to the eye. The zero-point energy amounts to 172 meV/atom for $P = 0$ and 207 meV/atom for $P = -0.5$ eV \AA^{-2} . The dashed line corresponds to the results obtained by Brito *et al.*⁵³ using the REBO potential. Note that $1 \text{ eV } \text{\AA}^{-2} = 16 \text{ N m}^{-1}$ in SI units.

In fact, A does not present a negative thermal expansion, as happens for the in-plane area in a large temperature range^{11,59} (see below). The difference $A - A_p$ increases with temperature, as bending of the graphene sheet increases, but even for $T \rightarrow 0$, A and A_p are not exactly equal, due to zero-point motion of the C atoms in the transverse z direction.

III. ENERGY AND ENTHALPY

A. Internal energy

The internal energy E is obtained from the results of our PIMD simulations as a sum of the kinetic, K , and potential energy, V , at a given temperature. The kinetic energy has been calculated by employing the virial estimator,⁶⁴ which displays a statistical uncertainty smaller than the potential energy. We have included in E the center-of-mass translational energy, a classical magnitude amounting to $E_{\text{CM}} = 3k_B T/2$ at temperature T . This quantity is irrelevant for the energy per atom in large systems, but we have included it to minimize finite size effects.¹¹

We express the internal energy as $E = E_0 + V + K$, taking as energy reference the value E_0 corresponding to the equilibrium configuration of a planar graphene surface in a classical approach at $T = 0$ (minimum-energy configuration of the considered LCBOPII potential, without quantum atomic delocalization). This corresponds to

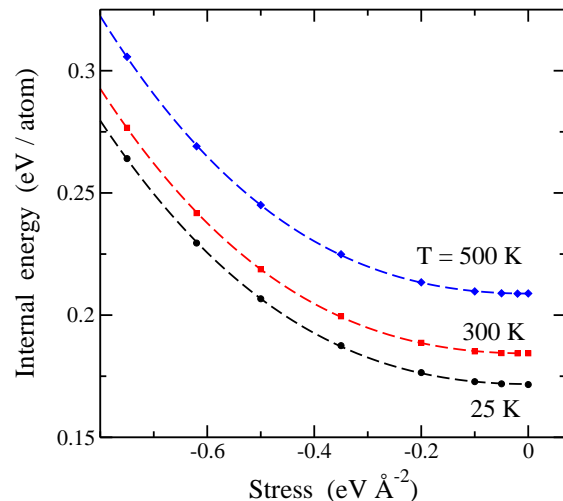


FIG. 2: Stress dependence of the internal energy of graphene for three temperatures: $T = 25$ (circles), 300 (squares), and 500 K (diamonds). Symbols indicate simulation results and lines are fits to the expression $E - E_0 = c_0 + c_2 P^2 + c_3 P^3$.

an interatomic distance $d_{\text{C-C}} = 1.4199 \text{ \AA}$, i.e., an area $A_0 = 2.6189 \text{ \AA}^2$ per atom. In a quantum approach, out-of-plane atomic fluctuations associated to zero-point motion appear even for $T \rightarrow 0$, and the graphene layer is not strictly planar. Moreover, anharmonicity of in-plane vibrations gives rise to a zero-point lattice expansion, yielding a distance $d_{\text{C-C}} = 1.4287 \text{ \AA}$, i.e., around 1% larger than the classical distance at $T = 0$.¹¹

In Fig. 1 we show the temperature dependence of the internal energy per atom, $E - E_0$, as derived from our PIMD simulations in the isothermal-isobaric ensemble for $P = 0$ (circles), -0.2 (squares), and -0.5 eV \AA^{-2} (diamonds). For $P = 0$ it was shown earlier that the size effect on the internal energy per atom is negligible for $N = 960$ (less than the symbol size in Fig. 1), as compared with the largest cells considered in Ref. 11. The zero-point energy, E_{ZP} , is found to be 172 meV/atom for $P = 0$, and slightly higher for -0.2 eV \AA^{-2} , but it appreciably increases for $P = -0.5$ eV \AA^{-2} to a value of 207 meV/atom. We will show later that this rise in internal energy is basically due to the elastic energy associated to an increase in the area A . For comparison with our results, we also present in Fig. 1 the energy $E - E_0$ obtained by Brito *et al.*⁵³ from path-integral Monte Carlo simulations using the REBO potential (dashed line). These authors called it vibrational energy, and corresponds to our internal energy; our vibrational energy E_{vib} is defined below (see Sec. III.C). The REBO potential yields a zero-point energy of 0.181 eV/atom, i.e., a 5% higher than that found here with the LCBOPII potential.

The rise in internal energy with an applied tensile stress is presented in Fig. 2 for three temperatures: $T = 25$ K (circles), 300 K (squares), and 500 K (diamonds). For zero stress we find at 25 K an internal energy very

close to that of the ground state E_{ZP} . In the stress range displayed in Fig. 2 the internal energy can be fitted to an expression $E - E_0 = c_0 + c_2 P^2 + c_3 P^3$, with a coefficient of the quadratic term $c_2 \approx 0.090 \text{ \AA}^4 \text{ eV}^{-1}$, nearly independent of the temperature. This is the leading term for the variation of internal energy with the applied pressure, which is nearly parabolic for stresses between 0 and -0.1 eV \AA^{-2} .

The change in internal energy with temperature and pressure can be described from variations in the elastic and vibrational contributions to E . This is analyzed in the following sections.

B. Elastic energy

An important part of the internal energy corresponds to the elastic energy due to changes in the area of graphene. It is directly related to the actual interatomic distance, i.e., to the real area A , rather than to the in-plane area A_p (or in-plane strain ϵ). Then, the internal energy $E(T)$ at temperature T can be written as¹¹

$$E(T) = E_0 + E_{\text{el}}(A) + E_{\text{vib}}(A, T), \quad (5)$$

where $E_{\text{el}}(A)$ is the elastic energy for an area A , and $E_{\text{vib}}(A, T)$ is the vibrational energy of the system. The area A is a function of the stress P and temperature T , but this is not explicitly indicated in Eq. (5) for simplicity of the notation. One expects non-zero values of the elastic energy, even in the absence of an externally applied stress, due to thermal expansion at finite temperatures, as well as for zero-point expansion at $T = 0$. $E_{\text{vib}}(A, T)$ is given by contributions of phonons in graphene, both in-plane and out-of-plane vibrational modes.

We define the elastic energy E_{el} corresponding to an area A as the increase in energy of a strictly planar graphene layer with respect to the minimum energy E_0 (for an area $A_0 = 2.61888 \text{ \AA}^2/\text{atom}$). By definition $E_{\text{el}}(A_0) = 0$, and for small changes of A we found that it follows a dependence $E_{\text{el}}(A) \approx K(A - A_0)^2$, with $K = 2.41 \text{ eV \AA}^{-2}$. This dependence for $E_{\text{el}}(A)$ yields a 2D bulk modulus $B_0 = A_0(\partial^2 E_{\text{el}}/\partial A^2) = 2KA_0$, i.e., $B_0 = 12.6 \text{ eV \AA}^{-2}$, in agreement with the result found earlier in classical calculations at $T = 0$.²⁰

Our PIMD simulations directly yield $E(T)$, which can be split into an elastic and a vibrational part, as in Eq. (5). At room temperature ($T \sim 300 \text{ K}$) and for small stresses P (A close to A_0), the elastic energy is much smaller than the vibrational energy E_{vib} , but this can be different for low T and/or large applied stresses (see below).

In Fig. 3 we display the temperature dependence of the elastic energy, as derived from our PIMD simulations for $P = 0$, -0.2 , and -0.5 eV \AA^{-2} . For a given external stress, E_{el} increases with T , as a consequence of the thermal expansion of the real area A , which turns out to be positive for all temperatures $T > 0$ ($\alpha > 0$, see below). Note that, in contrast, the in-plane area A_p

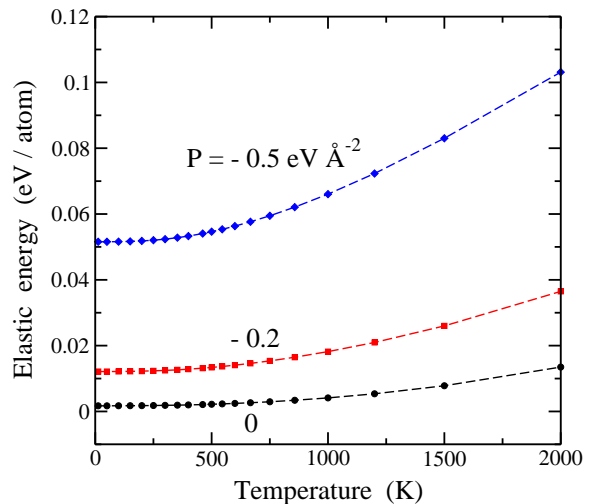


FIG. 3: Temperature dependence of the elastic energy E_{el} of graphene, as derived from the real area A obtained in PIMD simulations for $P = 0$ (circles), -0.2 (squares), and -0.5 eV \AA^{-2} (diamonds). Symbols represent simulation results and error bars are less than the symbol size. Dashed lines are guides to the eye.

displays a thermal contraction ($\alpha_p < 0$) in a wide temperature range, so that it is not a suitable candidate for a reliable definition of the elastic energy.

For $P = 0$ we find a positive elastic energy in the zero-temperature limit, $E_{\text{el}} = 1.7 \text{ meV/atom}$, due to zero-point lattice expansion, which causes that $A > A_0$. This low- T limit appreciably increases for $P < 0$ due to the stress-induced increase in area A , which yields values of 12 and 52 meV/atom for the elastic energy at $P = -0.2$ and -0.5 eV \AA^{-2} , respectively. For finite temperatures, one observes in Fig. 3 that $E_{\text{el}}(T)$ increases faster with temperature for larger tensile stress. This is due to an increase in the graphene compressibility (reduction of the elastic constants) for rising tensile stress, which in turn causes an increase in the thermal expansion coefficient α (see Sec. IV).

C. Vibrational energy

After calculating the elastic energy for an area A resulting from PIMD simulations at given T and P , we obtain the vibrational energy $E_{\text{vib}}(A, T)$ by subtracting the elastic energy from the internal energy: $E_{\text{vib}} = E(T) - E_0 - E_{\text{el}}(A)$ (see Eq. (5)). In Fig. 4 we present the temperature dependence of the vibrational energy of graphene for $P = 0$ (circles), -0.2 (squares), and -0.5 eV \AA^{-2} (diamonds), as derived from our simulations. In contrast to Figs. 1 and 3, where one observes that E and E_{el} increase with the applied tensile stress P , in Fig. 4 one sees that the vibrational energy is lower for higher tensile stress. This is mainly due to a decrease

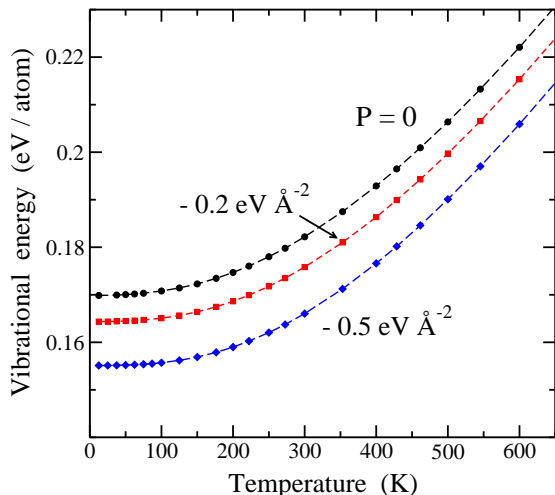


FIG. 4: Temperature dependence of the vibrational energy per atom, E_{vib} , for $P = 0$ (circles), -0.2 (squares), and -0.5 $\text{eV} \text{ \AA}^{-2}$ (diamonds). Error bars are less than the symbol size. Dashed lines are guides to the eye.

in the vibrational frequency of in-plane modes for increasing stress (increasing area), corresponding to positive Grünesien parameters.^{39,74}

The zero-point vibrational energy is found to decrease from 170 meV/atom for $P = 0$ to 164 and 155 meV/atom for $P = -0.2$ and -0.5 $\text{eV} \text{ \AA}^{-2}$, respectively. This decrease, although clearly noticeable, is smaller than the increase of about 50 meV/atom in the elastic energy for $P = -0.5$ $\text{eV} \text{ \AA}^{-2}$ (see Fig. 3). These zero- T energy values per atom correspond in a harmonic approximation to $\langle 3\hbar\omega/2 \rangle$, which is a mean value for the frequencies ω in the six phonon bands of graphene.^{75,76} Our results for $P = 0$ correspond to $\langle \omega \rangle = 914$ cm^{-1} , to be compared with 833 cm^{-1} for $P = -0.5$ $\text{eV} \text{ \AA}^{-2}$.

The three curves for $E_{\text{vib}}(T)$ shown in Fig. 4 for different stresses are roughly parallel in the displayed temperature range. Values of E_{vib} presented in this figure are clearly larger than those corresponding to a classical model for the vibrational modes. In this limit, the vibrational energy per atom is $E_{\text{vib}}^{\text{cl}} = 3k_B T/2$, which means 39 and 78 meV/atom for $T = 300$ and 600 K, respectively. In contrast, we find $E_{\text{vib}} = 166$ and 206 meV/atom from PIMD simulations for $P = -0.5$ $\text{eV} \text{ \AA}^{-2}$ at those temperatures.

We note that in the language of membranes and 2D elastic media there appears an energy contribution due to bending of the surface, that is usually taken into account through the bending constant κ , which measures the rigidity of the membrane. In our present formulation, the bending energy is included in the vibrational energy associated to the flexural ZA modes, as can be seen in their contribution to the specific heat (see Sec. V). Anharmonic couplings between in-plane and out-of-plane modes are also expected to show up, especially at high

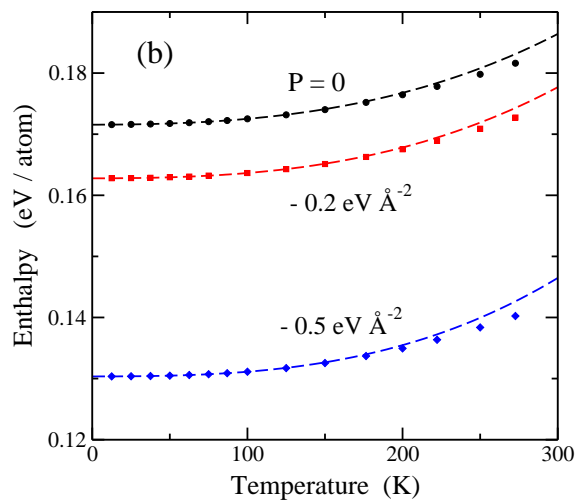
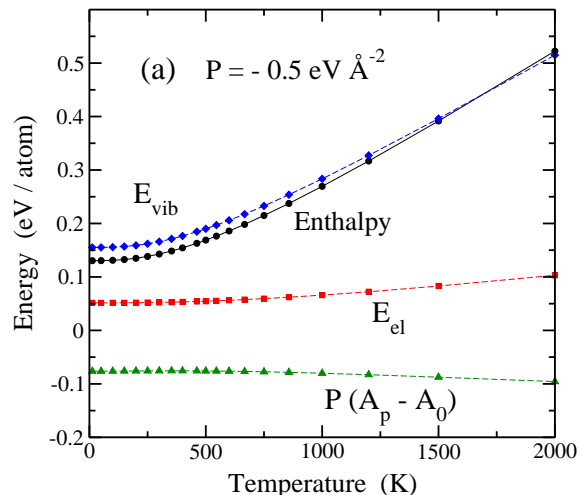


FIG. 5: Enthalpy per atom, $H - H_0$, as a function of temperature. (a) Enthalpy for a tensile stress $P = -0.5$ $\text{eV} \text{ \AA}^{-2}$ (circles), along with its three components, E_{vib} , E_{el} , and $P(A_p - A_0)$ (see Eq. (6)). Dashed lines are guides to the eye. (b) Enthalpy in the low-temperature region for $P = 0$ (circles), -0.2 (squares), and -0.5 $\text{eV} \text{ \AA}^{-2}$ (diamonds). Symbols represent results of PIMD simulations. Error bars are less than the symbol size. Dashed lines in (b) indicate fits of the simulation results to the polynomial $H - H_0(P) = H_{\text{ZP}} + a_2 T^2 + a_3 T^3$ in the region from $T = 0$ to 100 K.

temperatures.⁷⁷

D. Enthalpy

Since we are working in the isothermal-isobaric ensemble, it is natural to consider the enthalpy as a relevant

thermodynamic variable, in particular to calculate the specific heat of graphene at several applied stresses (see Sec. V). For a given stress P , we define the enthalpy H as $H = E + PA_p$. As a reference we will consider $H_0(P) = E_0 + PA_0$, such that H converges in the classical limit to $H_0(P)$ at $T = 0$.

In Fig. 5(a) we present the enthalpy of graphene, $H - H_0(P)$, as a function of temperature for a tensile stress $P = -0.5 \text{ eV } \text{\AA}^{-2}$. Results of our simulations are displayed as circles. Taking into account that the enthalpy can be written as

$$H - H_0(P) = E_{\text{el}} + E_{\text{vib}} + P(A_p - A_0), \quad (6)$$

we have plotted in Fig. 5(a) the temperature dependence of the three contributions in the r.h.s. of Eq. (6). The largest change with temperature appears for the vibrational energy (diamonds). The elastic energy, E_{el} , as well as the term $P(A_p - A_0)$ are also found to depend on temperature, due to the thermal expansion (or contraction) of the in-plane area A_p , but their change is much smaller than that of E_{vib} . As a result, the enthalpy turns out to be smaller than the vibrational energy at low temperature, because $E_{\text{el}} + P(A_p - A_0) < 0$. However, $H - H_0(P)$ becomes larger than E_{vib} at $T \gtrsim 1500 \text{ K}$, due to the larger increase in E_{el} for rising temperature.

To better appreciate the low-temperature region, in Fig. 5(b) we present the temperature dependence of the enthalpy, as derived from PIMD simulations up to $T = 300 \text{ K}$. Symbols indicate results of the simulations for $P = 0$ (circles), -0.2 (squares), and $-0.5 \text{ eV } \text{\AA}^{-2}$ (diamonds). Dashed lines are fits to the expression $H - H_0(P) = H_{2P} + a_2 T^2 + a_3 T^3$ in the temperature region from $T = 0$ to 100 K . This polynomial form shows good agreement with the temperature dependence of the enthalpy obtained from the simulations in the fitted region. For $T \gtrsim 150 \text{ K}$, the lines depart progressively from the data points. Note that a linear term in this expression for the enthalpy is not allowed for thermodynamic consistency, since the specific heat $c_p = (\partial H / \partial T)_P$ has to vanish in the limit $T \rightarrow 0$. The coefficient a_2 changes from $6.1 \times 10^{-8} \text{ eV K}^{-2}$ for $P = 0$ to $2.6 \times 10^{-8} \text{ eV K}^{-2}$ for $P = -0.5 \text{ eV } \text{\AA}^{-2}$. The coefficient a_3 varies from 3.5 to $5.1 \times 10^{-10} \text{ eV K}^{-3}$ in the same stress range. This is important for the low-temperature dependence of the specific heat discussed in Sec. V, as the contribution of the quadratic coefficient a_2 decreases for increasing stress, whereas a_3 is found to increase. This means that the specific heat c_p in the lowest temperatures accessible to our simulation method will be given as a combination of a linear term $2a_2 T$ and a quadratic one $3a_3 T^2$, with the latter becoming more important for larger tensile stresses.

IV. THERMAL EXPANSION

In the low-temperature limit ($T \rightarrow 0$), the real area A and in-plane area A_p derived from PIMD simulations

converge to $2.6459 \text{ \AA}^2/\text{atom}$ and $2.6407 \text{ \AA}^2/\text{atom}$, respectively. Comparing these values with the classical minimum $A_0 = 2.6189 \text{ \AA}^2$, we find a zero-point expansion in A and A_p of about $0.02 \text{ \AA}^2/\text{atom}$ ($\sim 1\%$), due to an increase in the mean C-C bond length (an anharmonic effect). There also appears a difference of 0.2% between real and in-plane areas at low temperature, caused by out-of-plane zero-point motion, so that the layer is not strictly planar. This is a genuine quantum effect, as in classical simulations for $T \rightarrow 0$ one finds a planar layer in which A and A_p coincide.^{11,20} The difference $A - A_p$ increases as temperature is raised, since A_p is the projection of A on the xy reference plane, and the real graphene surface becomes increasingly bent for rising temperature because of larger out-of-plane atomic displacements.

For $P = 0$, the area A displays an almost constant value up to $T \approx 200 \text{ K}$, and increases at higher temperatures. However, A_p decreases in the temperature range from $T = 0$ to $T \approx 1000 \text{ K}$, reaches a minimum and then increases at higher T .¹¹ These results for A_p are qualitatively similar to those found from classical Monte Carlo and molecular dynamics simulations of graphene,^{59,73} but in PIMD simulations the contraction of A_p with respect to the zero-temperature value is significantly larger than for classical calculations.

To analyze the thermal expansion of graphene, and following our definitions of the areas A and A_p , we will consider two different thermal expansion coefficients. The first of them, α , refers to changes in the real area:

$$\alpha = \frac{1}{A} \left(\frac{\partial A}{\partial T} \right)_P \quad (7)$$

This coefficient takes mainly into account changes in the interatomic distances, and is rather insensitive to bending of the graphene layer. The second coefficient, α_p , is a measure of variations in the in-plane area and has been widely used in the literature to analyze results of classical simulations and analytical calculations:

$$\alpha_p = \frac{1}{A_p} \left(\frac{\partial A_p}{\partial T} \right)_P. \quad (8)$$

In Fig. 6 we present both thermal expansion coefficients, as derived from our PIMD simulations for $P = 0$ (circles), -0.2 (squares), and $-0.5 \text{ eV } \text{\AA}^{-2}$ (diamonds). Symbols are data points obtained from numerical derivatives of the areas A (panel a) and A_p (panel b). For these derivatives we took temperature intervals ranging from 10 K at low temperature to about 50 K at temperatures $T \sim 1000 \text{ K}$. In general, the statistical uncertainty (error bars) in the values of α_p obtained from numerical derivatives is larger than that found for α , as a consequence of the larger fluctuations in A_p . The behavior of α shown in Fig. 6(a) is similar to that observed for most 3D materials, i.e., it goes to zero in the low-temperature limit and increases for rising temperature so that $\alpha > 0$ for $T > 0$.^{74,78} This is related to the fact that the in-plane vibrational modes have positive Grüneisen parameters

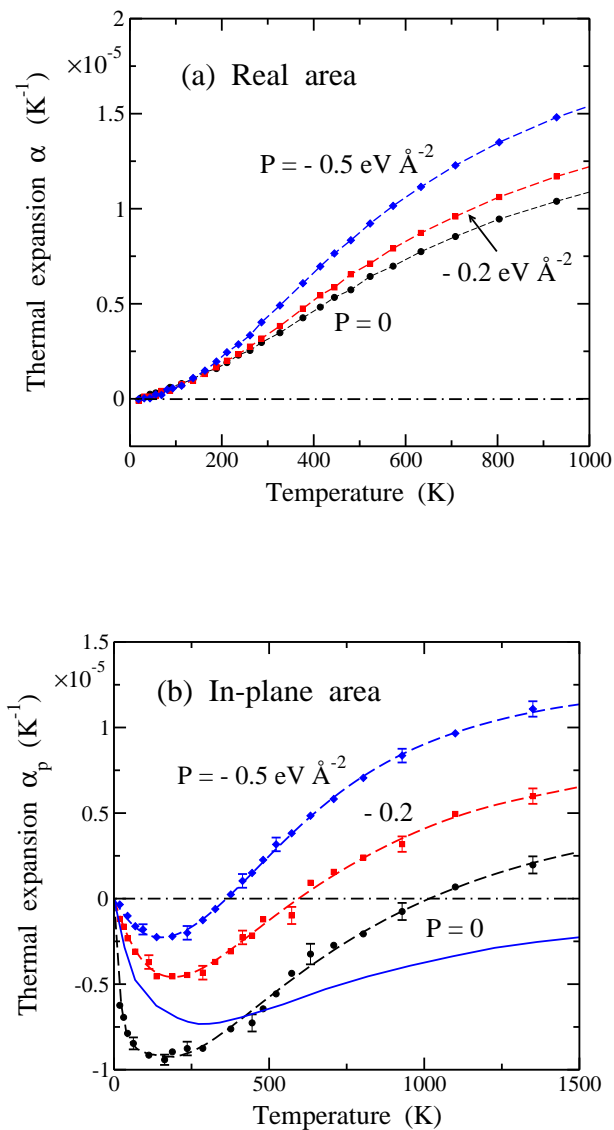


FIG. 6: (a) Thermal expansion coefficient α of graphene vs temperature, as derived from the results of PIMD simulations. (b) In-plane thermal expansion coefficient α_p of graphene vs temperature, obtained from numerical derivatives of the area A_p . In both panels, symbols represent data points for different stresses: $P = 0$ (circles), -0.2 (squares), and -0.5 eV \AA^{-2} (diamonds). Dashed lines are polynomial fits to the data points. The solid line indicates the result obtained in Ref. 39 from density-functional perturbation theory.

when they are calculated with respect to the real area A . One observes in Fig. 6(a) that α is higher for larger tensile stress. In fact, at 800 K the α value obtained for $P = -0.5 \text{ eV \AA}^{-2}$ is 40% larger than that corresponding to $P = 0$. Viewing the thermal expansion as an anharmonic effect, this can be interpreted as an increase in anharmonicity for larger tensile stress. This is associated with an increase in area A and the corresponding decrease in the frequency of vibrational in-plane modes,

which in turn causes a larger vibrational amplitude and consequently a larger anharmonicity.

The in-plane thermal expansion coefficient α_p also converges to zero in the low-temperature limit, but contrary to α it decreases for increasing temperature until reaching a minimum, as shown in Fig 6(b). The negative value of α_p in the minimum approaches zero for rising tensile stress. In fact, it goes from $-9.2 \times 10^{-6} \text{ K}^{-1}$ for $P = 0$ to $-2.3 \times 10^{-6} \text{ K}^{-1}$ for $P = -0.5 \text{ eV \AA}^{-2}$. At higher T , α_p approaches zero and eventually becomes positive at a temperature T_0 , which changes appreciably with the applied stress. As a result, we find $T_0 = 1020, 590 \text{ K}$, and $360(\pm 10) \text{ K}$, for the three values of the stress P presented in Fig. 6.

It is interesting to note that the difference $\alpha - \alpha_p$, which vanishes at $T = 0$, rapidly increases for rising temperature, and for $P = 0$ it takes a value $\approx 1.0 \times 10^{-5} \text{ K}^{-1}$ at temperatures higher than 1000 K. For larger tensile stress, this difference is smaller, since the amplitude of out-of-plane vibrations is reduced, and A_p is closer to A . Thus, for $P = -0.2$ and -0.5 eV \AA^{-2} , we find at high temperatures $\alpha - \alpha_p \approx 8 \times 10^{-6} \text{ K}^{-1}$ and $6.5 \times 10^{-6} \text{ K}^{-1}$, respectively.

The results presented here for α_p at zero external stress display a temperature dependence similar to those found earlier using other theoretical and experimental techniques.^{37,79–81} The solid line in Fig. 6(b) represents the thermal expansion coefficient α_p obtained by Mounet and Marzari³⁹ from DFT combined with a QHA for the vibrational modes. Similar curves $\alpha_p(T)$ were obtained from first-principles calculations in Refs. 40,41, converging to negative values at high temperature. This seems to be a drawback of this kind of calculations, which are optimal to obtain the total energy and electronic structure of the system, but the employed QHA may be not precise enough to capture the important coupling between in-plane and out-of-plane vibrational modes at relatively high temperatures. This mode coupling controls the in-plane thermal expansion.

Jiang *et al.*⁷⁹ studied free-standing graphene using a nonequilibrium Green's function approach, and obtained a minimum for α_p of about -10^{-5} K^{-1} , similar to our data for $P = 0$ displayed in Fig. 6(b). Moreover, these authors found a crossover from negative to positive α_p for a temperature $T_0 \sim 600 \text{ K}$, lower than the results of our PIMD simulations. An even lower temperature $T_0 \sim 400 \text{ K}$ has been found by using other theoretical techniques.^{37,82} Room-temperature Raman measurements⁸¹ yielded $\alpha_p = -8 \times 10^{-6} \text{ K}^{-1}$, whereas a value of $-7 \times 10^{-6} \text{ K}^{-1}$ was derived from scanning electron microscopy.⁸⁰ We note, however, that the agreement between measurements with different techniques is not so good for the temperature dependence of α_p , since the change in α_p at $T > 300 \text{ K}$ is faster in the former case⁸¹ than in the latter.⁸⁰

The temperature dependence of α_p can be qualitatively understood as a competition between two opposing factors. On one side, the real area A increases as T is raised

in the whole temperature range considered here. On the other side, bending of the graphene surface causes a decrease in its projection, A_p , onto the xy plane. For stress-free graphene at temperatures $T \lesssim 1000$ K, the decrease due to out-of-plane vibrations is larger than the thermal expansion of the real surface, and $\alpha_p < 0$. For $T \gtrsim 1000$ K, the thermal expansion of A dominates over the contraction of A_p associated to out-of-plane atomic motion, and thus $\alpha_p > 0$. For graphene under tensile stress, the amplitude of out-of-plane vibrations is smaller, so the decrease in A_p is also smaller and the region of negative α_p is reduced.

Our results for the thermal expansion of graphene, derived from atomistic simulations, can be related with an analytical formulation of crystalline membranes in the continuum limit, for which the relation between A and A_p may be written as^{20,72}

$$A = \int_{A_p} dx dy \sqrt{1 + (\nabla h(x, y))^2}. \quad (9)$$

Here $h(x, y)$ is the height of the membrane surface, i.e. the distance to the reference xy plane. In this classical approach, the difference $A - A_p$ may be calculated by Fourier transformation of the r.h.s. of Eq. (9).^{15,20,25} In this procedure one needs to consider a dispersion relation $\omega_{ZA}(\mathbf{k})$ for out-of-plane modes (ZA flexural band), where $\mathbf{k} = (k_x, k_y)$ are 2D wavevectors. The frequency dispersion in this acoustic band is well approximated by the expression $\rho\omega_{ZA}^2 = \sigma k^2 + \kappa k^4$, consistent with an atomic description of graphene²⁸ ($k = |\mathbf{k}|$; ρ , surface mass density; σ , effective stress; κ , bending modulus). Then, for effective stress $\sigma > 0$, which is the case at finite temperatures, even for zero external stress ($P = 0$), one finds^{20,28}

$$A = A_p \left[1 + \frac{k_B T}{8\pi\kappa} \ln \left(1 + \frac{2\pi\kappa}{\sigma A_p} \right) \right]. \quad (10)$$

This expression was obtained in the classical limit, so it does not take into account atomic quantum delocalization. Nevertheless, it is expected to be a good approximation to our quantum calculations at relatively high temperature, $T \gtrsim \Theta_D$, with $\Theta_D \sim 1000$ K the Debye temperature corresponding to out-of-plane vibrations in graphene.^{83,84}

We note that both κ and σ change with temperature and stress, so that it is not straightforward to write down an analytical formula for $\alpha - \alpha_p$ from a temperature derivative of Eq. (10). For given temperature T and stress $\sigma = \sigma_0 - P$ we can write $A - A_p = \delta A_p T$, δ being a parameter derived from Eq. (10), which is a good approximation for the difference $\alpha - \alpha_p$. The effective stress σ_0 appears at finite temperatures for zero external stress ($P = 0$), and vanishes for $T \rightarrow 0$ in the classical limit.²⁸ Introducing the finite-temperature values of σ_0 and κ given earlier,^{20,28} we find $\delta = 1.0 \times 10^{-5} \text{ K}^{-1}$, $6.6 \times 10^{-6} \text{ K}^{-1}$, and $5.1 \times 10^{-6} \text{ K}^{-1}$ for $P = 0$, -0.2 , and $-0.5 \text{ eV } \text{\AA}^{-2}$, respectively. These values are close to those found for $\alpha - \alpha_p$ from our PIMD simulations (see above). However, the difference between both sets of results increases

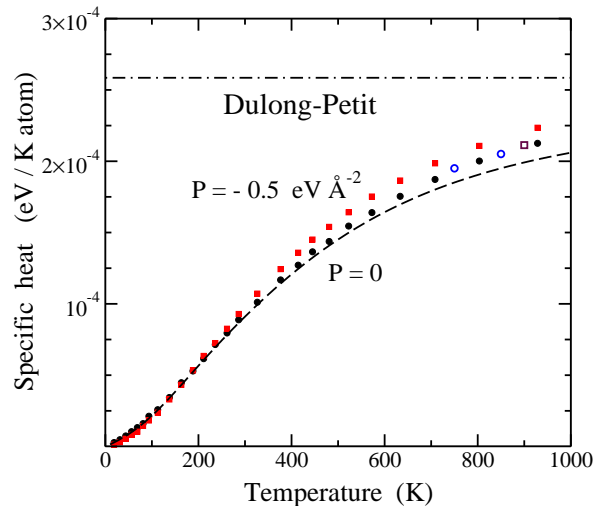


FIG. 7: Specific heat of graphene as a function of temperature, as derived from PIMD simulations for $P = 0$ (circles) and $-0.5 \text{ eV } \text{\AA}^{-2}$ (squares). Error bars of the data points are less than the symbol size. The dashed line is the specific heat c_v obtained from the six phonon bands corresponding to the LCBOP potential in a harmonic approximation ($P = 0$). Open symbols indicate results for c_v derived from DFT-type calculations at $T = 900$ K (square, Ref. 34), 850 K and 750 K (circles, Ref. 35). The horizontal dashed-dotted line represents the classical Dulong-Petit limit.

for rising tensile stress. Thus, for $P = -0.5 \text{ eV } \text{\AA}^{-2}$ our simulations yield $\alpha - \alpha_p = 6.5 \times 10^{-6} \text{ K}^{-1}$, larger than the prediction based on Eq. (10), which is based on harmonic vibrations. We observe that the importance of anharmonic effects (including also quantum corrections) is manifested more clearly for large tensile stresses.

V. SPECIFIC HEAT

We have calculated the specific heat of graphene monolayers as a temperature derivative of the enthalpy H derived from our PIMD simulations (see Sec. III.D): $c_p(T) = dH(T)/dT$. One may ask if our simulations can yield reliable results for this thermodynamic variable, mainly because electronic contributions to c_p are not taken into account in our numerical procedure. This is, however, not a problem for the actual precision reached in our calculations, as the electronic part is much less than the phonon contribution, actually considered in our method. The former was estimated in various works, and turns out to be three or four orders of magnitude less than the phonon part in the temperature range considered here.^{33,85,86}

In Fig. 7 we display the specific heat of graphene as a function of temperature for $P = 0$ (circles) and $-0.5 \text{ eV } \text{\AA}^{-2}$ (squares), as obtained from a numerical derivative of the enthalpy. For comparison, the classical Dulong-Petit specific heat is shown as a dashed-dotted line ($c_v^{\text{cl}} = 3k_B$).

At room temperature the specific heat of graphene is about three times smaller than the classical limit, and c_p is still appreciably lower than this limit at $T = 1000$ K. This is in line with the magnitude of the Debye temperature of graphene, which amounts to about 1000 K for out-of-plane modes^{83,84} and $\Theta_D \gtrsim 2000$ K for in-plane vibrations.^{31,83} In Fig. 7 we also present results for c_v at $P = 0$ taken from earlier DFT calculations combined with a QHA: $T = 900$ K from Ref. 34 (open square), 850 K and 750 K from Ref. 35 (open circles). These data agree well with the results of our PIMD simulations.

For a comparison with our numerical results for $c_p(T)$ at zero and negative stress, we present a harmonic approximation (HA) for the lattice vibrations. This approximation is expected to be rather accurate at low temperatures, provided that a reliable description for the phonon frequencies is used. A comparison between results of the HA and PIMD simulations yields an estimate of anharmonic effects in the specific heat of graphene, given that both kinds of calculations employ the same interatomic potential.

The HA assumes constant frequencies for the graphene vibrational modes (calculated for the minimum-energy configuration), and does not take into account changes in the areas A and A_p with temperature. Thus, it will give us the constant-area specific heat per atom, $c_v(T) = dE(T)/dT$, which for a cell with N atoms is given by

$$c_v(T) = \frac{k_B}{N} \sum_{r,\mathbf{k}} \frac{[\frac{1}{2}\beta\hbar\omega_r(\mathbf{k})]^2}{\sinh^2[\frac{1}{2}\beta\hbar\omega_r(\mathbf{k})]}, \quad (11)$$

where the index r ($r = 1, \dots, 6$) indicates the six phonon bands of graphene (ZA, ZO, LA, TA, LO, and TO),^{39,75,76} and the sum in \mathbf{k} runs over wavevectors $\mathbf{k} = (k_x, k_y)$ in the hexagonal Brillouin zone, with discrete \mathbf{k} points spaced by $\Delta k_x = 2\pi/L_x$ and $\Delta k_y = 2\pi/L_y$.²⁸ For increasing system size N , one has new long-wavelength modes with an effective cut-off $\lambda_{max} \approx L$, with $L = (NA_p)^{1/2}$, and the minimum wavevector is $k_0 = 2\pi/\lambda_{max}$ (i.e., $k_0 \sim N^{-1/2}$).

The dashed line in Fig. 7 was calculated with the HA using Eq. (11), with the frequencies $\omega_r(\mathbf{k})$ ($r = 1, \dots, 6$) obtained from diagonalization of the dynamical matrix corresponding to the LCBOPH potential. Results of the simulations for $P = 0$ follow closely the HA up to about 400 K, and they become progressively higher than the dashed line at higher temperatures, for which anharmonic effects become more important. At room temperature ($T = 300$ K) we obtained $c_v = 9.1 \times 10^{-5}$ eV/K atom from the HA vs a value of $9.3(\pm 0.1) \times 10^{-5}$ eV/K atom derived from PIMD simulations. Both values are a little higher than that found by Ma *et al.*³⁵ from DFT calculations ($c_v = 8.6$ J/K mol, i.e. 8.9×10^{-5} eV/K atom). The difference between results obtained for $P = 0$ from *ab-initio* calculations combined with a QHA and those presented here for a simpler HA are due to two main reasons. The first reason is that in the HA one does not take into account changes of frequencies with the temperature,

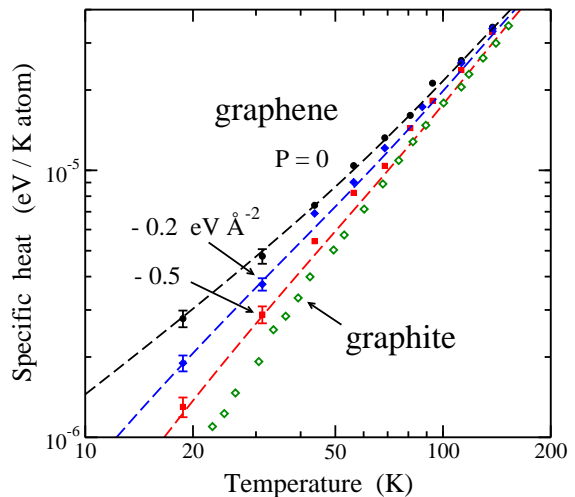


FIG. 8: Specific heat of graphene as a function of temperature. Symbols represent results derived from PIMD simulations for $P = 0$ (circles), -0.2 (diamonds), and -0.5 eV \AA^{-2} (squares). Lines were derived from a HA based on the six phonon bands corresponding to the LCBOPH potential for $N = 61440$ (see text for details). Experimental data for graphite obtained by Desorbo and Tyler⁹⁰ are shown as open diamonds.

and the second is the relative inaccuracy of the phonon bands derived from the considered effective potential far from the Γ point, as compared with those obtained from DFT calculations. The HA provides, however, a consistency check for the results of the PIMD simulations at low temperature, as discussed below.

As shown in Sec. III, a part of the internal energy (and the enthalpy) corresponds to the elastic energy E_{el} , i.e., to the cost of increasing the area A of graphene by thermal expansion or an applied tensile stress. The contribution of this energy to the specific heat is given by dE_{el}/dT , which is not included in the HA. This contribution can be calculated from the results of our PIMD simulations displayed in Fig. 3. For $P = 0$, it amounts to 2.3 and 5.5×10^{-6} eV/K atom at 500 and 1000 K, which means a nonnegligible increase in the specific heat with respect to the pure HA. This increase is especially visible at $T \gtrsim 500$ K, capturing part of the anharmonicity of the system. In fact, at $T = 1000$ K it accounts for a 45% of the difference between the results derived from PIMD simulations and the HA presented in Fig. 7. The rest of that difference is associated to anharmonicity of the lattice vibrations.

In our present context, the most relevant effect of an applied stress P in the phonon bands is a change in the low-frequency region of the ZA modes, for which

$$\omega_{ZA}(\mathbf{k})^2 = \omega_{ZA}^0(\mathbf{k})^2 - \frac{P}{\rho} k^2 \quad (12)$$

The zero-stress band $\omega_{ZA}^0(\mathbf{k})$ calculated for the minimum-energy structure (area A_0), follows for small k :

$\rho\omega_{\text{ZA}}^0(\mathbf{k})^2 \approx \kappa k^4$. Thus, for $P < 0$ the small- k region is dominated by the quadratic term (linear in P) in Eq. (12), and $\omega_{\text{ZA}}(\mathbf{k}) \approx \sqrt{-P/\rho} k$ for $k \ll 1 \text{ \AA}^{-1}$. The specific heat of stressed graphene in the HA has been calculated by taking the frequencies $\omega_{\text{ZA}}(\mathbf{k})$ derived from Eq. (12).

To obtain deeper insight into the low-temperature dependence of the specific heat, $c_p(T)$ is shown in Fig. 8 in a logarithmic plot. Symbols indicate results derived from PIMD simulations for $P = 0$ (circles), -0.2 (squares), and -0.5 eV \AA^{-2} (diamonds). With our present method, we cannot give reliable values of c_p for temperatures lower than 15 K, mainly due to the very large computation times required for Trotter numbers $N_{\text{Tr}} > 500$. Dashed lines show $c_v(T)$ derived from the harmonic approximation using Eq. (11) for a large cell size ($N = 61440$ atoms). Such a large N cannot be reached in our quantum simulations, and gives us a useful reference where finite-size effects are minimized. The lines corresponding to the HA follow closely the data points derived from the simulations at low temperatures. For $P = -0.5 \text{ eV \AA}^{-2}$ one observes that the PIMD results become progressively higher than the HA line at $T > 50 \text{ K}$. Such a difference is almost unobservable for $P = -0.2 \text{ eV \AA}^{-2}$, and disappears for $P = 0$. It is clear that the HA describes well the specific heat in the stress-free case at $T < 200 \text{ K}$, and becomes less accurate as tensile stress and/or temperature increase.

The low-temperature behavior of the heat capacity can be further analyzed by considering a continuous model for frequencies and wavevectors, as in the well-known Debye model for solids.⁷⁴ At low-temperatures, c_v is mainly controlled by the contribution of acoustic modes with small k . For graphene, these are TA and LA modes with $\omega_r \propto k$, and ZA flexural modes with quadratic dispersion ($\omega_r \propto k^2$) for negligible σ at $P = 0$ and low T , whereas it is linear in k for $P < 0$. In general, the low- T contribution of a phonon branch with dispersion relation $\omega_r \propto k^n$ can be approximated by replacing the sum in Eq. (11) by an integral, which yields $c_v^r \sim T^{2/n}$ (see Ref. 61). We note that for d -dimensional systems one finds an exponent d/n .^{87,88}

Summarizing the above comments, the low-temperature contributions of the relevant phonon branches to the specific heat (those with $\omega(k) \rightarrow 0$ for $k \rightarrow 0$), one has for graphene $c_v \sim T^\mu$ close to $T = 0$, with $\mu = 1$ for $P = 0$ and $\mu = 2$ in the presence of a tensile stress ($P < 0$). This is in fact what we find for c_v from the HA at low temperature in our calculations for a large graphene supercell. To see the convergence of μ to its low- T value, we have calculated this exponent as a function of temperature from a logarithmic derivative: $\mu = d \ln c_v / d \ln T$. Close to $T = 0$ we obtain the values expected from our discussion above, but in the region displayed in Fig. 8, μ has not yet reached the zero-temperature value. In fact, for $T = 10 \text{ K}$ we find for μ the values 1.05, 1.59, and 1.85, for $P = 0$, -0.2 , and -0.5 eV \AA^{-2} , respectively. The first of them is already

close to its low-temperature limit ($\mu = 1$), but the exponents for graphene under stress are still somewhat lower than their zero- T limit ($\mu = 2$). We note that the larger the tensile stress (larger $\sigma = \sigma_0 - P$), the closer is μ to 2 at a relatively low T , since the wavenumber region where the linear term dominates in the $\omega(k)$ dispersion of the ZA band is larger ($\rho\omega_{\text{ZA}}^2 \approx \sigma k^2$). For the results of our PIMD simulations we note that, although one can obtain an exponent μ from a linear fit in the logarithmic plot of Fig. 8 (in particular the fit is rather good for $T < 100 \text{ K}$), it is true that the actual slope is slowly changing in this temperature range.

Alofi and Srivastava⁸⁹ calculated the specific heat of few-layer graphene by using a semicontinuum model and analytical expressions for phonon dispersion relations. In particular, for single-layer graphene they found a temperature dependence $c_v \sim T^{1.1}$ for $T \gtrsim 10 \text{ K}$, with an exponent that coincides with the mean μ value derived from our results for $P = 0$ in the region from 10 to 50 K.

For comparison with our results for graphene, we also present in Fig. 8 experimental data for the specific heat c_p of graphite, obtained by Desorbo and Tyler.⁹⁰ For graphite, the dependence of c_p on temperature has been analyzed in detail over the years.⁹¹⁻⁹⁴ For $T < 10 \text{ K}$, c_p rises as T^3 (a temperature region not shown in Fig. 8), as in the Debye model, and for temperatures between 10 and 100 K, it increases as T^2 ($\mu = 2$). The major difference with stress-free graphene is that in graphite the dominant contribution to c_p in this temperature range arises from phonons with a linear dispersion relation for small k ($\omega \sim k$). At room temperature the experimental specific heat of graphite is $8.90 \times 10^{-5} \text{ eV/K atom}$ (8.59 J/K mol), somewhat less than the result for graphene derived from our PIMD simulations for $P = 0$: $c_p = 9.3(\pm 0.1) \times 10^{-5} \text{ eV/K atom}$.

To compare with the results for c_p of graphene derived from our PIMD simulations, we have also calculated the specific heat c_v from constant- A_p simulations. For each considered temperature, we took the equilibrium area A_p obtained in the isothermal-isobaric simulations, and calculated c_v as a numerical derivative of the internal energy

$$c_v = \left(\frac{\Delta E}{\Delta T} \right)_{A_p} \quad (13)$$

from temperature increments ΔT (both positive and negative). One expects that $c_v \leq c_p$ at any temperature, but the difference between them turns out to be less than the statistical error bars of our results. A realistic estimation of this difference can be obtained from the thermodynamic relation^{61,95}

$$c_p - c_v = \frac{T\alpha_p^2 A_p}{\chi_p} \quad (14)$$

where χ_p is the in-plane isothermal compressibility (see Sec. VI). Using Eq. (14), we find that $c_p - c_v$ is at least two orders of magnitude less than the c_p values given above for the tensile stresses and temperatures considered here.

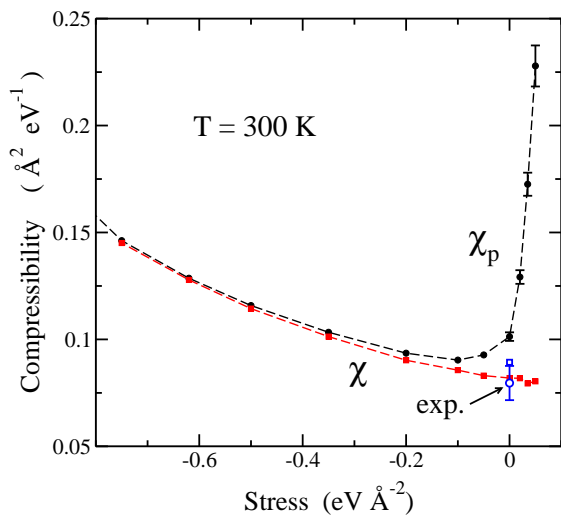


FIG. 9: Stress dependence of the isothermal compressibilities χ (squares) and χ_p (circles) of graphene at $T = 300$ K, as derived from PIMD simulations. Error bars, when not shown, are in the order of the symbol size. Open symbols indicate results derived from AFM indentation experiments: a square from Ref. 98 and a circle from Ref. 6 (the error bar corresponds to one standard deviation for several measurements).

We finally note that a calculation of the low- T specific heat of solids using this kind of path-integral simulations is in general not straightforward. The verification of the Debye law $c_p \sim T^3$ has been a challenge for path-integral simulations of 3D materials, because of the effective low-frequency cut-off corresponding to finite simulation cells.^{96,97} This kind of calculations at relatively low temperatures are in principle more reliable for 2D materials due to two different reasons. The first reason is that the length of the cell sides scales as $N^{1/d}$, and the minimum wavevector k_0 available in the simulations is $k_0 \sim N^{-1/d}$. For a simulation cell including N atoms, k_0 is less for 2D than for 3D materials, so that the low-frequency region is represented better for $d = 2$, and therefore the low-temperature regime will be also better described. The second reason is that the internal energy (or enthalpy) for graphene rises as $T^{\mu+1}$ with $\mu = 2$ or 3. At low T , this increase is faster than the usual phonon contribution to the enthalpy in 3D materials ($H \sim T^4$), and consequently it is more readily observable (less relative statistical noise) for 2D materials such as graphene.

VI. COMPRESSIBILITY

The in-plane isothermal compressibility is defined as

$$\chi_p = -\frac{1}{A_p} \left(\frac{\partial A_p}{\partial P} \right)_T. \quad (15)$$

The variables in the r.h.s. of this equation refer to in-plane quantities, as the pressure P in our isothermal-

isobaric ensemble is a variable conjugate to the in-plane area A_p . χ_p has been calculated here by using the fluctuation formula^{20,95}

$$\chi_p = \frac{N\sigma_p^2}{k_B T A_p} \quad (16)$$

where σ_p^2 are the mean-square fluctuations of the area A_p obtained in the simulations. This expression is more convenient for our purposes than obtaining $(\partial A_p / \partial P)_T$, since a calculation of this derivative by numerical methods requires additional simulations at nonzero stresses. We have verified at some selected temperatures and pressures that both procedures give the same results for χ_p (taking into account the statistical error bars). Similarly, for the real area A one can define a compressibility $\chi = -(\partial A / \partial P)_T / A$, which will be related to the fluctuations of the real area A .

In Fig. 9 we present the stress dependence of the compressibilities χ_p (circles) and χ (squares) of graphene, as derived from our PIMD simulations at 300 K. At $P = 0$, one finds $\chi_p > \chi$, as a consequence of the larger fluctuations in the in-plane area A_p . In this figure we have included some points corresponding to (small) compressive stresses $P > 0$, to remark the very different behavior of χ_p and χ in this region. χ follows a regular dependence, in the sense that it displays a smooth change as P is varied in the considered stress region. The in-plane compressibility χ_p , however, increases fast for $P > 0$, which is consistent with an eventual divergence at a critical stress P_c . This divergence of χ_p shows the same fact as the vanishing of the in-plane bulk modulus B_p (the inverse of χ_p) discussed in Ref. 20 from classical calculations. Close to this critical compressive stress the planar morphology of graphene becomes unstable due to large fluctuations in the in-plane area, which is related to the onset of imaginary frequencies in the ZA phonon bands for $P > P_c$. A detailed characterization of this wrinkling transition at P_c is out of the scope of this paper and will be investigated further in the near future. It is not yet clear whether quantum effects may be relevant or not for a precise definition of P_c . It is remarkable that the compressibility χ derived from the real area does not display any abrupt change in the region close to the critical stress, as both the area A and its fluctuations are rather insensitive to the corrugation of the graphene surface imposed by compressive stresses. For large tensile stress, χ and χ_p converge one to the other, as shown in Fig. 9, since the amplitude of out-of-plane vibrations becomes smaller and the real graphene surface is closer to the reference xy plane.

For comparison with the results of our simulations, we also present in Fig. 9 data for the compressibility of graphene at $P = 0$ derived from atomic force microscopy (AFM) indentation experiments. We have transformed the values for the Young modulus Y given in Refs. 6,98 to compressibility by using the expression $\chi = 2(1 - \nu)/Y$, with a Poisson ratio $\nu = 0.15$.²⁰ The resulting compressibilities are plotted as open symbols: a square⁹⁸

and a circle⁶ (the error bar indicates one standard deviation for several measurements). We note that interferometric profilometry experiments¹⁹ have revealed that close to $P = 0$ much smaller values of the Young modulus (much larger compressibilities) can be found for graphene. These authors have suggested that this apparent discrepancy can be associated to the difference between compressibilities of the real and projected areas, as discussed here. It seems that some experimental techniques can measure one of them, while other techniques may be sensitive to the other. This is an ongoing discussion that should be elucidated in the near future.^{20,27}

A thermodynamic parameter related to the thermal expansion α_p and compressibility χ_p is the dimensionless Grüneisen parameter γ , defined as

$$\gamma = \frac{\sum_{r\mathbf{k}} \gamma_{r\mathbf{k}} c_{vr}(\mathbf{k})}{\sum_{r\mathbf{k}} c_{vr}(\mathbf{k})}, \quad (17)$$

where $c_{vr}(\mathbf{k})$ is the contribution of mode $(r\mathbf{k})$ to the specific heat, and $\gamma_{r\mathbf{k}}$ are mode-dependent Grüneisen parameters.^{39,74} The overall γ can be related with our in-plane variables in graphene by using the thermodynamic relation^{61,74}

$$\gamma = \frac{\alpha_p A_p}{\chi_p c_v}. \quad (18)$$

For $P = 0$, the results of our PIMD simulations yield $\gamma = -2.2$ at 300 K, and at 1000 K, $\gamma \approx 0$ within the precision of the numerical results. At $T = 300$ K, α_p and γ are negative because the mode-dependent Grüneisen parameter of the out-of-plane ZA modes is negative.^{4,34,39} However, for $T > 1000$ K, this negative contribution is dominated by the positive sign of $\gamma_{r\mathbf{k}}$ for in-plane modes, which are excited at these temperatures, so that α_p and γ are positive.

At room temperature ($T = 300$ K) we find $\gamma = -1.2$ and -0.24 , for $P = -0.2$ and -0.5 eV \AA^{-2} , respectively. Although these values of γ are still negative, they are very different from the zero-stress result ($\gamma = -2.2$). Looking at Eq. (18), the main reason for this important change in the Grüneisen parameter with tensile stress is the large variation in the in-plane thermal expansion coefficient α_p , which takes values of -8.5 , -3.9 , and -1.0×10^{-6} K⁻¹ for $P = 0$, -0.2 , and -0.5 eV \AA^{-2} , respectively (see Fig. 6(b)). From the point of view of the phonon contributions to γ , the small negative value found for $P = -0.5$ eV \AA^{-2} indicates that the relative contribution of phonons with negative $\gamma_{r\mathbf{k}}$ (out-of-plane ZA modes) is at room temperature less important than for $P = 0$. This is due to an increase in frequency of small- k modes ($\omega_{ZA} \sim \sqrt{-P/\rho} k$), which causes a reduction in its corresponding $c_{vr}(\mathbf{k})$ at 300 K (see Eq. (17)).

VII. SUMMARY

In this paper we have presented and discussed results of PIMD simulations of graphene in a wide range of temper-

atures and tensile stresses. This technique has allowed us to quantify several structural and thermodynamic properties, with particular emphasis on the thermal expansion and specific heat. Nuclear quantum effects are clearly appreciable in these variables, even at T higher than room temperature. Zero-point expansion of the graphene layer due to nuclear quantum motion is not negligible, and amounts to about 1% of the area A . This zero-point effect decreases as tensile stress is increased.

The thermal contraction of graphene discussed in the literature turns out to be a reduction of the in-plane area A_p ($\alpha_p < 0$), caused by out-of-plane vibrations, but not a decrease in the real area A . In fact, the difference $A - A_p$ rises as temperature increases, since the amplitude of those vibrations grows. On one side, the in-plane thermal expansion α_p is negative at low temperature, and becomes positive for $T \gtrsim 1000$ K. On the other side, the thermal expansion α of the real area is positive for all temperatures and tensile stresses discussed here. The thermal contraction of A_p is smaller as the tensile stress increases, due to a reduction in the amplitude of out-of-plane vibrations. Our PIMD simulations give $\alpha_p < 0$ at low T for stresses so high as -0.5 eV \AA^{-2} (-8 N/m). For this stress, α_p becomes positive at $T \sim 350$ K.

The anharmonicity of the vibrational modes is clearly noticeable in the behavior of A and A_p . The increase in real area A for rising T ($\alpha > 0$) is a consequence of anharmonicity of in-plane modes, similar to the thermal expansion in most 3D solids. Moreover, the peculiar dependence of α_p (negative at low T and positive at high T) is an indication of the coupling between in-plane and out-of-plane modes.

Other thermal properties of graphene can be well described by an HA at relatively low T , once the frequencies of the vibrational modes are known for the classical equilibrium geometry at $T = 0$. This is the case of the specific heat, for which our PIMD results indicate that the effect of anharmonicity appears gradually for temperatures $T \gtrsim 400$ K. Part of this anharmonicity is due to the elastic energy E_{el} , associated to the expansion of the actual graphene sheet, which is not taken into account by the HA. At low T the specific heat can be described as $c_p \sim T^\mu$. At the lowest temperatures studied here ($T \gtrsim 10$ K) we find an exponent $\mu = 1.05$ and 1.85 , for $P = 0$ and -0.5 eV \AA^{-2} , respectively. These values are close to the corresponding low-temperature ($T \rightarrow 0$) values, i.e., $\mu = 1$ for stress-free and $\mu = 2$ for stressed graphene.

We note the consistency of the simulation results with the principles of thermodynamics, in particular with the third law. This means that thermal expansion coefficients have to vanish for $T \rightarrow 0$, as found for both the in-plane area A_p and the real area A derived from our simulations for $P = 0$ and $P < 0$. The same happens for the specific heat, i.e., $c_p \rightarrow 0$ for $T \rightarrow 0$.

Acknowledgments

The authors acknowledge the help of J. H. Los in the implementation of the LCBOPII potential. This work

was supported by Dirección General de Investigación, MINECO (Spain) through Grants FIS2012-31713 and FIS2015-64222-C2.

-
- ¹ A. K. Geim and K. S. Novoselov, *Nature Mater.* **6**, 183 (2007).
 - ² R. Roldan, L. Chirolli, E. Prada, J. Angel Silva-Guillen, P. San-Jose, and F. Guinea, *Chem. Soc. Rev.* **46**, 4387 (2017).
 - ³ A. H. Castro Neto, F. Guinea, N. M. R. Peres, K. S. Novoselov, and A. K. Geim, *Rev. Mod. Phys.* **81**, 109 (2009).
 - ⁴ A. A. Balandin, *Nature Mater.* **10**, 569 (2011).
 - ⁵ S. Ghosh, I. Calizo, D. Teweldebrhan, E. P. Pokatilov, D. L. Nika, A. A. Balandin, W. Bao, F. Miao, and C. N. Lau, *Appl. Phys. Lett.* **92**, 151911 (2008).
 - ⁶ C. Lee, X. Wei, J. W. Kysar, and J. Hone, *Science* **321**, 385 (2008).
 - ⁷ R. Prasher, *Science* **328**, 185 (2010).
 - ⁸ J. H. Seol, I. Jo, A. L. Moore, L. Lindsay, Z. H. Aitken, M. T. Pettes, X. Li, Z. Yao, R. Huang, D. Broido, et al., *Science* **328**, 213 (2010).
 - ⁹ J. C. Meyer, A. K. Geim, M. I. Katsnelson, K. S. Novoselov, T. J. Booth, and S. Roth, *Nature* **446**, 60 (2007).
 - ¹⁰ A. Fasolino, J. H. Los, and M. I. Katsnelson, *Nature Mater.* **6**, 858 (2007).
 - ¹¹ C. P. Herrero and R. Ramírez, *J. Chem. Phys.* **145**, 224701 (2016).
 - ¹² C. R. Woods, L. Britnell, A. Eckmann, R. S. Ma, J. C. Lu, H. M. Guo, X. Lin, G. L. Yu, Y. Cao, R. V. Gorbachev, et al., *Nature Phys.* **10**, 451 (2014).
 - ¹³ B. Amorim, A. Cortijo, F. de Juan, A. G. Grushine, F. Guinea, A. Gutierrez-Rubio, H. Ochoa, V. Parente, R. Roldan, P. San-Jose, et al., *Phys. Rep.* **617**, 1 (2016).
 - ¹⁴ E. Evans and W. Rawicz, *Phys. Rev. Lett.* **64**, 2094 (1990).
 - ¹⁵ S. A. Safran, *Statistical Thermodynamics of Surfaces, Interfaces, and Membranes* (Addison Wesley, New York, 1994).
 - ¹⁶ E. Cerda and L. Mahadevan, *Phys. Rev. Lett.* **90**, 074302 (2003).
 - ¹⁷ Y. W. Wong and S. Pellegrino, *J. Mech. Materials Struct.* **1**, 3 (2006).
 - ¹⁸ D. A. Kirilenko, A. T. Dideykin, and G. Van Tendeloo, *Phys. Rev. B* **84**, 235417 (2011).
 - ¹⁹ R. J. T. Nicholl, H. J. Conley, N. V. Lavrik, I. Vlassiouk, Y. S. Puzyrev, V. P. Sreenivas, S. T. Pantelides, and K. I. Bolotin, *Nature Commun.* **6**, 8789 (2015).
 - ²⁰ R. Ramírez and C. P. Herrero, *Phys. Rev. B* **95**, 045423 (2017).
 - ²¹ G. López-Polín, M. Jaafar, F. Guinea, R. Roldán, C. Gómez-Navarro, and J. Gómez-Herrero, *Carbon* **124**, 42 (2017).
 - ²² W. Helfrich and R. M. Servuss, *Nuovo Cimento D* **3**, 137 (1984).
 - ²³ J.-B. Fournier and C. Barbetta, *Phys. Rev. Lett.* **100**, 078103 (2008).
 - ²⁴ P. Tarazona, E. Chacón, and F. Bresme, *J. Chem. Phys.* **139**, 094902 (2013).
 - ²⁵ E. Chacón, P. Tarazona, and F. Bresme, *J. Chem. Phys.* **143**, 034706 (2015).
 - ²⁶ M. Pozzo, D. Alfè, P. Lacovig, P. Hofmann, S. Lizzit, and A. Baraldi, *Phys. Rev. Lett.* **106**, 135501 (2011).
 - ²⁷ R. J. T. Nicholl, N. V. Lavrik, I. Vlassiouk, B. R. Srijanto, and K. I. Bolotin, *Phys. Rev. Lett.* **118**, 266101 (2017).
 - ²⁸ R. Ramírez, E. Chacón, and C. P. Herrero, *Phys. Rev. B* **93**, 235419 (2016).
 - ²⁹ D. Nelson, T. Piran, and S. Weinberg, *Statistical Mechanics of Membranes and Surfaces* (World Scientific, London, 2004).
 - ³⁰ B. Amorim, R. Roldan, E. Cappelluti, A. Fasolino, F. Guinea, and M. I. Katsnelson, *Phys. Rev. B* **89**, 224307 (2014).
 - ³¹ E. Pop, V. Varshney, and A. K. Roy, *MRS Bull.* **37**, 1273 (2012).
 - ³² P. Wang, W. Gao, and R. Huang, *J. Appl. Phys.* **119**, 074305 (2016).
 - ³³ K. C. Fong, E. E. Wollman, H. Ravi, W. Chen, A. A. Clerk, M. D. Shaw, H. G. Leduc, and K. C. Schwab, *Phys. Rev. X* **3**, 041008 (2013).
 - ³⁴ S. Mann, P. Rani, R. Kumar, G. S. Dubey, and V. K. Jindal, *RSC Adv.* **6**, 12158 (2016).
 - ³⁵ F. Ma, H. B. Zheng, Y. J. Sun, D. Yang, K. W. Xu, and P. K. Chu, *Appl. Phys. Lett.* **101**, 111904 (2012).
 - ³⁶ A. Alofi and G. P. Srivastava, *Phys. Rev. B* **87**, 115421 (2013).
 - ³⁷ A. L. C. da Silva, L. Candido, J. N. Teixeira Rabelo, G. Q. Hai, and F. M. Peeters, *EPL* **107**, 56004 (2014).
 - ³⁸ I. S. Burmistrov, I. V. Gornyi, V. Y. Kachorovskii, M. I. Katsnelson, and A. D. Mirlin, *Phys. Rev. B* **94**, 195430 (2016).
 - ³⁹ N. Mounet and N. Marzari, *Phys. Rev. B* **71**, 205214 (2005).
 - ⁴⁰ C. Sevik, *Phys. Rev. B* **89**, 035422 (2014).
 - ⁴¹ S. Mann, R. Kumar, and V. K. Jindal, *RSC Adv.* **7**, 22378 (2017).
 - ⁴² F. Shimojo, R. K. Kalia, A. Nakano, and P. Vashishta, *Phys. Rev. B* **77**, 085103 (2008).
 - ⁴³ P. L. de Andres, F. Guinea, and M. I. Katsnelson, *Phys. Rev. B* **86**, 245409 (2012).
 - ⁴⁴ G. M. Chechin, S. V. Dmitriev, I. P. Lobzenko, and D. S. Ryabov, *Phys. Rev. B* **90**, 045432 (2014).
 - ⁴⁵ C. P. Herrero and R. Ramírez, *Phys. Rev. B* **79**, 115429 (2009).
 - ⁴⁶ E. Cadelano, P. L. Palla, S. Giordano, and L. Colombo, *Phys. Rev. Lett.* **102**, 235502 (2009).
 - ⁴⁷ E. Akatyeva and T. Dumitrica, *J. Chem. Phys.* **137**, 234702 (2012).
 - ⁴⁸ G.-D. Lee, E. Yoon, N.-M. Hwang, C.-Z. Wang, and K.-M. Ho, *Appl. Phys. Lett.* **102**, 021603 (2013).
 - ⁴⁹ Y. Magnin, G. D. Foerster, F. Rabilloud, F. Calvo, A. Zappelli, and C. Bichara, *J. Phys.: Condens. Matter* **26**, 185401 (2014).
 - ⁵⁰ J. H. Los, A. Fasolino, and M. I. Katsnelson, *Phys. Rev.*

- Lett. **116**, 015901 (2016).
- ⁵¹ M. J. Gillan, Phil. Mag. A **58**, 257 (1988).
- ⁵² D. M. Ceperley, Rev. Mod. Phys. **67**, 279 (1995).
- ⁵³ B. G. A. Brito, L. Cândido, G.-Q. Hai, and F. M. Peeters, Phys. Rev. B **92**, 195416 (2015).
- ⁵⁴ R. P. Feynman, *Statistical Mechanics* (Addison-Wesley, New York, 1972).
- ⁵⁵ C. P. Herrero and R. Ramírez, J. Phys.: Condens. Matter **26**, 233201 (2014).
- ⁵⁶ C. Cazorla and J. Boronat, Rev. Mod. Phys. **89**, 035003 (2017).
- ⁵⁷ J. H. Los, L. M. Ghiringhelli, E. J. Meijer, and A. Fasolino, Phys. Rev. B **72**, 214102 (2005).
- ⁵⁸ L. M. Ghiringhelli, J. H. Los, E. J. Meijer, A. Fasolino, and D. Frenkel, Phys. Rev. Lett. **94**, 145701 (2005).
- ⁵⁹ K. V. Zakharchenko, M. I. Katsnelson, and A. Fasolino, Phys. Rev. Lett. **102**, 046808 (2009).
- ⁶⁰ A. Politano, A. R. Marino, D. Campi, D. Farías, R. Miranda, and G. Chiarello, Carbon **50**, 4903 (2012).
- ⁶¹ C. P. Herrero and R. Ramírez, J. Chem. Phys. **148**, 102302 (2018).
- ⁶² P. Lambin, Appl. Sci. **4**, 282 (2014).
- ⁶³ H. Shiba, H. Noguchi, and J.-B. Fournier, Soft Matter **12**, 2373 (2016).
- ⁶⁴ M. E. Tuckerman and A. Hughes, in *Classical and Quantum Dynamics in Condensed Phase Simulations*, edited by B. J. Berne, G. Ciccotti, and D. F. Coker (World Scientific, Singapore, 1998), p. 311.
- ⁶⁵ M. E. Tuckerman, B. J. Berne, G. J. Martyna, and M. L. Klein, J. Chem. Phys. **99**, 2796 (1993).
- ⁶⁶ M. E. Tuckerman, B. J. Berne, and G. J. Martyna, J. Chem. Phys. **97**, 1990 (1992).
- ⁶⁷ G. J. Martyna, A. Hughes, and M. E. Tuckerman, J. Chem. Phys. **110**, 3275 (1999).
- ⁶⁸ G. J. Martyna, M. E. Tuckerman, D. J. Tobias, and M. L. Klein, Mol. Phys. **87**, 1117 (1996).
- ⁶⁹ C. P. Herrero, R. Ramírez, and E. R. Hernández, Phys. Rev. B **73**, 245211 (2006).
- ⁷⁰ C. P. Herrero and R. Ramírez, J. Chem. Phys. **134**, 094510 (2011).
- ⁷¹ R. Ramírez, N. Neuerburg, M. V. Fernández-Serra, and C. P. Herrero, J. Chem. Phys. **137**, 044502 (2012).
- ⁷² Q. Waheed and O. Edholm, Biophys. J. **97**, 2754 (2009).
- ⁷³ W. Gao and R. Huang, J. Mech. Phys. Solids **66**, 42 (2014).
- ⁷⁴ N. W. Ashcroft and N. D. Mermin, *Solid State Physics* (Saunders College, Philadelphia, 1976).
- ⁷⁵ L. J. Karssemeijer and A. Fasolino, Surf. Sci. **605**, 1611 (2011).
- ⁷⁶ L. Wirtz and A. Rubio, Solid State Commun. **131**, 141 (2004).
- ⁷⁷ V. M. Adamyan, V. N. Bondarev, and V. V. Zavalniuk, Phys. Lett. A **380**, 3732 (2016).
- ⁷⁸ C. P. Herrero and R. Ramírez, Phys. Rev. B **63**, 024103 (2000).
- ⁷⁹ J.-W. Jiang, J.-S. Wang, and B. Li, Phys. Rev. B **80**, 205429 (2009).
- ⁸⁰ W. Bao, F. Miao, Z. Chen, H. Zhang, W. Jang, C. Dames, and C. N. Lau, Nature Nanotech. **4**, 562 (2009).
- ⁸¹ D. Yoon, Y.-W. Son, and H. Cheong, Nano Lett. **11**, 3227 (2011).
- ⁸² K. H. Michel, S. Costamagna, and F. M. Peeters, Phys. Status Solidi B **252**, 2433 (2015).
- ⁸³ V. K. Tewary and B. Yang, Phys. Rev. B **79**, 125416 (2009).
- ⁸⁴ A. Politano, B. Borca, M. Minniti, J. J. Hinarejos, A. L. Vazquez de Parga, D. Farias, and R. Miranda, Phys. Rev. B **84**, 035450 (2011).
- ⁸⁵ L. X. Benedict, S. G. Louie, and M. L. Cohen, Solid State Commun. **100**, 177 (1996).
- ⁸⁶ T. Nihira and T. Iwata, Phys. Rev. B **68**, 134305 (2003).
- ⁸⁷ J. Hone, in *Carbon nanotubes: Synthesis, structure, properties, and applications*, edited by M. S. Dresselhaus, G. Dresselhaus, and P. H. Avouris (Springer, 2001), vol. 08 of *Topics in Applied Physics*, pp. 273–286.
- ⁸⁸ V. N. Popov, Phys. Rev. B **66**, 153408 (2002).
- ⁸⁹ A. Alofi and G. P. Srivastava, Appl. Phys. Lett. **104**, 031903 (2014).
- ⁹⁰ W. Desorbo and W. W. Tyler, J. Chem. Phys. **21**, 1660 (1953).
- ⁹¹ K. Komatsu and T. Nagamiya, J. Phys. Soc. Japan **6**, 438 (1951).
- ⁹² J. Krumhansl and H. Brooks, J. Chem. Phys. **21**, 1663 (1953).
- ⁹³ P. G. Klemens, Austr. J. Phys. **6**, 405 (1953).
- ⁹⁴ R. Nicklow, N. Wakabayashi, and H. G. Smith, Phys. Rev. B **5**, 4951 (1972).
- ⁹⁵ L. D. Landau and E. M. Lifshitz, *Statistical Physics* (Pergamon, Oxford, 1980), 3rd ed.
- ⁹⁶ J. C. Noya, C. P. Herrero, and R. Ramírez, Phys. Rev. B **53**, 9869 (1996).
- ⁹⁷ R. Ramírez, C. P. Herrero, and E. R. Hernández, Phys. Rev. B **73**, 245202 (2006).
- ⁹⁸ G. Lopez-Polin, C. Gomez-Navarro, V. Parente, F. Guinea, M. I. Katsnelson, F. Perez-Murano, and J. Gomez-Herrero, Nature Phys. **11**, 26 (2015).